

1 **Near real-time modelling of landslide impacts to inform rapid**
2 **response: an example from the 2016 Kaikōura, New Zealand,**
3 **earthquake**

4 Tom R. Robinson¹, Nick J. Rosser¹, Tim R.H. Davies², Thomas M. Wilson², Caroline Orchiston³

5 ¹Department of Geography, Institute of Hazard, Risk & Resilience, Durham University, Durham,
6 DH1 3LE, UK

7 ²Department of Geological Sciences, University of Canterbury, Christchurch, 8041, New
8 Zealand

9 ³Centre for Sustainability, University of Otago, Dunedin, 9016, New Zealand

10 *Correspondence to:* Tom R. Robinson (tom.robinson@durham.ac.uk)

11 **ABSTRACT**

12 Reliable methods to undertake near real-time modelling of landslide hazard and associated
13 impacts following an earthquake are required in order to provide crucial information to guide
14 emergency response. Following the 2016 Kaikōura earthquake in New Zealand, we undertook
15 such a near real-time modelling campaign in an attempt to pinpoint the location of landslides and
16 identify where roads and rivers had been blocked. The model combined an empirical analysis of
17 landslide hazard based on previously published global relationships with a simple runout model
18 based on landslide reach angles. It was applied manually with a first iteration completed within
19 24 hours of the earthquake, and a second iteration, based on updated shaking outputs, within ~ 72
20 hours. Both models highlighted that landsliding was expected to be widespread and that impacts
21 to roads were likely to mean Kaikōura township was cut-off. These results were used by

22 responders at the time to formulate aerial reconnaissance flight paths and to identify the risk of
23 landslide dams causing further damage. Subsequent model verification based on available
24 landslide inventories shows that while these models were able to capture a large percentage of
25 landslides and landslide impacts, the outputs were over-predicted, limiting their use for
26 pinpointing the precise locations of triggered landslides. To make future versions of the model
27 more useful for informing emergency response, continued work to modify and adapt the
28 approach to reduce this over-prediction is necessary. Nevertheless, the results from this study
29 show the model is a promising initial attempt at near real-time landslide modelling and efforts to
30 automate the approach would greatly increase the utility and speed of modelling in future
31 earthquakes.

32 **INTRODUCTION**

33 Landsliding during earthquakes in mountain regions is a widespread hazard that has previously
34 caused the majority of earthquake impacts to critical transport and utilities infrastructure (Bird &
35 Bommer, 2004). Such impacts are important during emergency response as they can impinge
36 access to affected regions, resulting in delays in search and rescue activities and the delivery of
37 aid. As well as obstructing infrastructure networks, landslides falling into rivers can emplace
38 landslide dams that block the river and cause upstream flooding. Catastrophic failure of these
39 dams can result in an outburst flood that can devastate downstream communities. Landslide
40 dams that fail typically do so soon after formation, with 41% of those that eventually fail, failing
41 within one week (Costa & Schuster, 1988). Pinpointing the locations where landslides block
42 transport routes and rivers post-earthquake in near real-time is therefore an important goal for
43 informing emergency response.

44 While a number of near real-time models of earthquake processes such as ground shaking
45 and resulting fatalities have been successfully developed (e.g. Jaiswal et al., 2009; Trendafiloski
46 et al., 2011), relatively little research has focussed on near real-time modelling of coseismic
47 landslides. Several recent methods have been attempted based either on a simplified Newmark
48 analysis (Jibson et al., 2000; Godt et al., 2008; 2009; Gallen et al., 2016) or using an empirical
49 approach (Nowicki et al., 2014; Kritikos et al., 2015; Robinson et al., 2017), but none are
50 currently operational and very few have been applied during a live earthquake response.
51 Approaches based on a simplified Newmark analysis combine information on ground shaking,
52 slope angle, and local material strength to assess the resulting slope deformation (Newmark,
53 1965). However, local material strength properties are rarely known, especially at scales relevant
54 to landslides, necessitating assumptions on rock strength and its variability, which can lead to
55 widely varying model outputs (Dreyfus et al., 2013; Gallen et al., 2016). These assumptions can
56 only be tested following the completion of event-specific landslide inventories, which can take
57 many months to complete (Williams et al., 2017).

58 Approaches using empirical analysis rely on observations of previous coseismic
59 landslides to ascertain the relationships between various predisposing factors and landslide
60 occurrence. Such models assume that the characteristics of locations where landslides have
61 previously been observed are representative of those where future landslides will occur.
62 Typically this approach has only been applied to a specific location; however, recent approaches
63 have attempted to use observations from multiple different locations to establish global
64 relationships (Nowicki et al., 2014; Kritikos et al., 2015; Marc et al., 2016; Parker et al., 2017).
65 However, in order to produce global relationships, such methods cannot consider local factors
66 like lithology or soil characteristics which are known to limit the accuracy of landslide models in

67 specific cases (Bozzano et al., 2008). Further uncertainties arise from studies that have shown
68 seasonal variations in slope failures during earthquakes (Chousianitis et al., 2016) that are also
69 not included in global relationships.

70 In this study, we describe a near real-time coseismic landslide modelling campaign
71 undertaken following the 2016 Kaikōura earthquake in New Zealand. This landslide hazard
72 modelling used an empirical approach based on adapted global relationships from Kritikos et al.
73 (2015). However, unlike previous attempts, our modelling also incorporated an analysis of the
74 risk landslides posed to major roads and rivers in the affected area using a simplified assessment
75 of potential reach angles. The results of these models were shared at the time with emergency
76 managers and science responders on the ground. Here, we describe the methods and results of
77 this near real-time modelling campaign along with quantitative analyses of model performance
78 based on available data. We discuss the rapidity with which this modelling was undertaken as
79 well as the resulting accuracy, and highlight the relative strengths and weaknesses of the
80 approach taken. Necessary improvements to further reduce the modelling time and increase the
81 model accuracy and utility are also discussed along with the potential to automate the method as
82 an add-on to other already available rapid earthquake modelling tools.

83 **SETTING**

84 **Earthquake and landslide hazard**

85 The Kaikōura earthquake occurred at 11:02 hrs on 13 November 2016 UTC (Coordinated
86 Universal Time) at a depth of 15 km and had a magnitude of M_w 7.8 (Fig. 1). The event
87 propagated northward for > 170 km in a complex rupture involving multiple previously known
88 and unknown faults (Hamling et al., 2017), making it one of the most complex earthquakes ever

89 recorded. Strong ground shaking of up to MMI IX was recorded along the entire rupture length
90 and consequently at least 10,000 landslides are thought to have occurred (Kaiser et al., 2017;
91 Dellow et al., 2017; Massey et al., This Issue). Along with fault surface rupture, landslides
92 caused extensive damage to transport infrastructure in the affected area (Fig. 1), in particular to
93 State Highway (SH) 1 and the Inland Kaikōura Road (Stirling et al., 2017; Davies et al., 2017).
94 This resulted in the isolation of Kaikōura township along with a number of other rural
95 communities in North Canterbury and southern Marlborough, leading to emergency air and sea
96 evacuations of > 600 stranded tourists (Davies et al., 2017). Road access to Blenheim and Picton
97 from Christchurch remained possible, but only via a > 200 km detour through steep mountain
98 passes (Fig. 1), adding over 7 hours to journey times. As well as damage to lifelines, > 190
99 landslide dams were formed (Fig. 1) throughout the affected area (Dellow et al., 2017). The
100 majority of these occurred in steep but small river catchments and consequently presented little
101 risk to local populations; however, at least 11 landslide dams were judged by regional Civil
102 Defence and Emergency Management (CDEM) groups to present a severe risk to downstream
103 populations and infrastructure.

104 **Transport infrastructure**

105 The region is steep and mountainous, rising from sea-level to over 2,500 m in ~ 20 km, with the
106 mountain ranges ending at the coast in steep cliffs. Despite this, the region is an important
107 transport corridor, particularly for freight and tourism. SH1 is the main arterial road access
108 between Christchurch and the tourist destinations of Kaikōura and Blenheim, traversing a narrow
109 corridor between the coast and mountains for > 100 km between Oaro and Ward (Fig. 1).
110 Alternative access between Christchurch and Kaikōura is possible via the Inland Kaikōura Road
111 (IKR), which passes through less steep terrain and connects to SH7, however no alternative road

112 access exists between Kaikōura and Blenheim. An alternative route between Christchurch and
113 Blenheim via SH7 adds an additional 200 km to the journey and passes through steep alpine
114 terrain (Fig. 1), making it unfavourable for heavy goods vehicles. This route is also vulnerable to
115 alpine hazards (Robinson et al., 2015) highlighting the lack of redundancy in the South Island
116 road network. The only other routes providing north-south access in this region are the Awatere
117 Valley Road and the Wairau-Hanmer Road, both of which are suitable for 4x4 vehicles only and
118 therefore provide emergency access only.

119 **Previous landslide impacts**

120 Given the mountainous nature of the South Island, temporary road closures due to landslides are
121 not uncommon, especially after earthquakes. A series of moderate earthquakes in 1994 caused
122 substantial damage to SH73, which is one of only three routes east-west across the Southern
123 Alps, closing the road for several days and restricting traffic for over one week (Paterson &
124 Bourne-Webb, 1994). Following the 2003 M_w 7.3 Fiordland earthquake, landslides caused minor
125 damage to several roads including SH94, which provides the only road access to Milford Sound
126 (Power et al., 2005). Most of these blockages resulted from small rockfalls and debris flows and
127 consequently were quickly cleared. The most extensive recent impacts to roads from landslides
128 were caused by the 2010-11 Canterbury earthquake sequence, which caused widespread damage
129 throughout the city of Christchurch (Bannister & Gledhill, 2012). Substantial rockfalls in the
130 Port Hills resulted in several road closures (Giovinazzi et al., 2011).

131 Landslide dams are common in New Zealand due to a combination of steep terrain,
132 narrow valleys, and high seismicity and rainfall. At least 232 landslide dams have been
133 documented, of which 39% are thought to have resulted from earthquakes, although the trigger
134 for a further 59% remains unexplained (Korup, 2004). While data on dam failures is thought to

135 be under-reported, Korup (2004) assessed the time to failure for those that did fail and suggested
136 that minimum decision-making times varied with dam volume, ranging from several minutes to
137 several days as volume increased. Generally, New Zealand was found to have larger volume
138 dams and impounded lakes than other mountainous regions.

139 **DATA & METHODS**

140 **Landslide hazard modelling**

141 The model employed following the Kaikōura earthquake was based on the empirical analysis
142 established by Kritikos et al. (2015). Their approach used fuzzy logic in GIS to combine the
143 effect of multiple predisposing factors, with the corresponding functions derived from
144 observations of the 1994 Northridge, 1999 Chi-Chi, and 2008 Wenchuan earthquakes. Robinson
145 et al. (2016a) later showed that the same functions also accurately modelled landslide hazard
146 from the 2003 and 2009 Fiordland earthquakes in southern New Zealand, confirming that the
147 approach was applicable more widely. Fuzzy logic-based approaches to landslide modelling have
148 previously been shown to match or out-perform other approaches (Pradhan, 2010; Bui et al.,
149 2012; Pourghasemi et al., 2012). However, most importantly for near real-time modelling, these
150 approaches are fast to apply, as much of the necessary input data can be derived and stored pre-
151 event (Fig. 2), reducing the amount of data collection required following an earthquake.

152 ***Fuzzy logic***

153 Fuzzy logic considers the role of multiple different factors influencing landslide occurrence, and
154 models how these different factors combine simultaneously to cause landslides from a specific
155 earthquake. Each predisposing factor is assigned a membership function, $\mu(x)$, that describes the

156 factor's relationship with landslide occurrence (e.g. increasing landslide frequency with
157 increasing slope angle) based on previous observations. These membership functions take values
158 [0, 1] where 0 represents the value of a given factor with the lowest frequency of landsliding, and
159 1 represents the highest frequency of landsliding. Each predisposing factor is therefore converted
160 into a fuzzy factor that effectively describes where landslides are more or less likely to occur as a
161 result of that individual factor. These fuzzy factors are then combined on a pixel-by-pixel basis
162 to establish the likelihood of landslides occurring in any given pixel from the specific earthquake
163 (i.e. landslide hazard). This combination of factors is a critical step in the process and
164 consequently various different combination approaches exist. However, for physical phenomena
165 such as landslides, the fuzzy gamma operator has been shown to be the most appropriate method
166 (Pradhan, 2010; Bui et al., 2012; Kritikos et al., 2015). Fuzzy gamma combines multiple factors
167 such that:

168

$$169 \quad L_{HZ} = \left[\prod_{F=1}^j \mu(x) \right]^{1-\gamma} \cdot \left[1 - \prod_{F=1}^j 1 - \mu(x) \right]^{\gamma} \quad (1)$$

170

171 where L_{HZ} represents landslide hazard, $\mu(x)$ is the membership function for factor F , j is the
172 number of factors to be combined, and γ is a constant. The value of γ strongly affects the output
173 L_{HZ} values, with Kritikos & Davies (2015) showing that the optimum value for landslide hazard
174 analysis was 0.9; smaller values consistently under-predicted landslide occurrence, while larger
175 values consistently over-predicted.

176 ***Hazard model parameters and data inputs***

177 The model requires inputs of local slope angle (*SA*), Modified Mercalli Intensity (*MMI*), slope
178 position (*SP*), fault proximity (*FD*), and river proximity (*RD*). Local slope angle, slope position,
179 and river proximity can all be readily obtained from a GDEM. Fault maps are available either
180 from local geologic agencies or from the global earthquake model (GEM) active fault database,
181 and *MMI* distribution can be calculated from a combination of ground motion prediction
182 equations, felt reports, and instrumental data within minutes of an earthquake occurring (Wald et
183 al., 2008; Horspool et al., 2015). We used the open-source Land Information New Zealand
184 (LINZ) national DEM (~ 25 m horizontal resolution) to calculate local slope angle and slope
185 position, as well as the LINZ river network to define river proximity. Fault locations were taken
186 from the GNS Science active fault database, which, at the time, did not include several of the
187 faults involved in the earthquake (Hamling et al., 2017; Stirling et al., 2017). *MMI* was taken
188 from two different sources: USGS ShakeMap®, and GeoNet earthquake records. This allowed
189 two versions of the model to be produced in near real-time, facilitating comparison between the
190 outputs to provide a degree of confidence around the results. The fact that several faults involved
191 in the rupture were not included in the active fault map available at the time is important, as
192 many landslides were subsequently found to have occurred very near to, or directly on these fault
193 ruptures (Massey et al., This Issue). Further, the initial USGS ShakeMap output that was used
194 did not account for such a complex rupture, instead basing shaking estimates on simple ground
195 motion prediction equations (GMPEs).

196 The membership functions for each factor used in this study are (Kritikos et al., 2015):

197

$$198 \quad \mu(SA) = \begin{cases} 0, SA \leq 15^\circ \\ 1/1 + (SA/4.875)^{-2.65}, SA > 15^\circ \end{cases} \quad (2)$$

$$199 \quad \mu(MMI) = 1/1 + (MMI/7.5)^{-14} \quad (3)$$

$$200 \quad \mu(FD) = 1/1 + (FD/2.375)^{5.375} \quad (4)$$

$$201 \quad \mu(RD) = 1/1 + (RD/3.25)^{5.5} \quad (5)$$

$$202 \quad \mu(SP) = 1/1 + (SP/2.325)^{-4.375} \quad (6)$$

203

204 Following the method of Kritikos et al. (2015), each factor was classified into different bins
 205 numbered consecutively from smallest to largest, with the bin number forming the input variable
 206 for the corresponding membership function (Table 1). We adapted the original membership
 207 function for slope angle to force slopes $\leq 15^\circ$ (bins 1-3) to have $\mu(x) = 0$, assuming no landslides
 208 will occur on these slopes. A simplified work flow showing the various input parameters and
 209 model steps is shown in Figure 2.

210 **Impact modelling**

211 *Danger pixels and landslide reach angle*

212 Modelling impacts resulting from landslides is a complex task due to difficulties in predicting
 213 landslide runout paths, amongst other factors. Several attempts have used an approach based on
 214 danger pixels, which identify the locations where impacts are likely based on the intersection
 215 between landslide hazard pixels and infrastructure pixels (Kanungo et al., 2008; Pellicani et al.,
 216 2014). These models typically use a semi-quantitative approach whereby landslide hazard is
 217 classified into zones of low, medium, high etc. with only the highest zones classified as danger
 218 pixels. Other attempts have focussed on using a simple horizon scanning approach to identify

219 network viewsheds in order to directly assess the risk to pre-existing and planned networks
220 (Robinson et al., 2016b), or to plan least-cost landslide-safe routes for new networks (Meinhardt
221 et al., 2015). However, in these approaches, all pixels within the viewshed are effectively
222 considered as danger pixels, irrespective of their corresponding landslide hazard or the reach
223 angle to the network concerned.

224 The reach angle, θ , of a landslide is an important measure of landslide mobility (Hsü,
225 1975; Hungr, 2006) and is derived from the angle of a line connecting the top of the landslide
226 scar to the distal toe of the deposit (Fig. 3). Calculating the reach angle between a specific
227 segment of a road/river network and the pixels within the corresponding viewshed therefore
228 identifies the relative mobility required for landslides in those viewshed pixels to intersect the
229 network segment (Fig. 3). Setting a minimum threshold reach angle that represents the largest
230 expected landslide mobility therefore identifies those pixels from which any landslide is
231 expected to have sufficient mobility to reach the network, i.e. the danger pixels, and eliminates
232 those pixels from which mobility is expected to be insufficient. The modelled landslide hazard
233 values within the corresponding danger pixels represent the likelihood of a landslide occurring,
234 and thus we therefore calculate the blockage risk based on the average modelled hazard values of
235 the danger pixels within a given network segment's corresponding viewshed. This ensures that
236 the only pixels contributing to the blockage risk calculation a) have runout directions broadly
237 towards the network; and b) have reach angles that suggest any landslide(s) will have sufficient
238 mobility to reach the network. This approach therefore improves upon previous approaches by
239 considering the potential mobility of landslides that occur as well as facilitating a fully
240 quantitative approach.

241 A key component of this approach is establishing the threshold reach angle. Several
242 studies have suggested that landslide reach angles are rarely $< 30^\circ$ (Hungr, 2006; Borella et al.,
243 2016); however, landslides with large volumes ($> 10^6 \text{ m}^3$) or flow-type mechanisms have been
244 shown to commonly have reach angles $< 30^\circ$ (Davies et al., 1999; Hungr, 1995; Legros, 2002),
245 with several examples of reach angles $< 5^\circ$ (e.g. Wadge et al., 1995). For the near real-time
246 modelling undertaken following the Kaikōura earthquake, a minimum threshold angle of 30° was
247 used; however, after the event, once data on landslide locations and impacts became available, a
248 sensitivity analysis of the effect of changing this threshold angle was performed.

249 *Loss model parameters and data inputs*

250 Calculating θ for each pixel in a viewshed with respect to a given segment of a network is a
251 simple task that can be undertaken rapidly. It requires comparing the elevation difference, H , and
252 the horizontal distance, L , between the network segment and each pixel in the corresponding
253 viewshed (Figs. 2 & 3) such that:

254

$$255 \theta = \tan^{-1} H/L \quad (7)$$

256

257 No measure of network vulnerability to landslides was included in the near real-time
258 analysis, with the results consequently only representing the likelihood of landslides reaching
259 and presumably obstructing the network. While vulnerability information may be important for
260 restoration estimates, longer term recovery planning, and estimating economic losses (Robinson
261 et al., 2015), at the time this analysis was undertaken it was thought the most pressing

262 information related to network obstruction. Nevertheless, future analyses may be able to account
263 for vulnerability.

264 Road and river centrelines were downloaded from the LINZ open-source data repository
265 and the horizontal distance from each network was calculated using the Euclidean Distance tool
266 in ESRI's ArcGIS. Only order 3 and above rivers were evaluated as a) the total number of order
267 1 and 2 rivers is extremely large and thus increases the total time required to complete
268 modelling; and b) landslide dams occurring on order 1 and 2 rivers were at the time considered
269 unlikely to present a substantial hazard due to the limited catchment size. The road network was
270 filtered to only include State Highways and other primary and emergency access roads, including
271 the Awatere Valley Road and the Wairau-Hanmer Road (Fig. 1). To reduce modelling time, both
272 networks were split into 1 km segments with danger pixels calculated for the mid-point of each
273 segment. This was thought to provide the best compromise between modelling speed and useful
274 output resolution. This resulted in 1,832 road segments and 8,456 river segments.

275 **Model application and distribution**

276 At the time of the Kaikōura earthquake, efforts to test, automate, and operationalise the model
277 (Fig. 2) were underway but had not yet been completed. However, the relative simplicity of the
278 approach combined with the availability of data allowed the modelling to be undertaken
279 manually. Modelling was undertaken remotely in the UTC time zone (13 hours behind New
280 Zealand Standard Time, NZST, at the time) on a single workstation using ESRI's ArcGIS.

281 The model results were made available to the New Zealand Science Advisory Group
282 (SAG), which was tasked with aiding both the scientific and emergency responses to the
283 earthquake and comprised various scientists from New Zealand's Universities and GNS Science
284 amongst others (Woods et al., 2017). Results were initially uploaded to a closed access

285 geospatial portal (*Engineering Response to the M7.8 Kaikōura earthquake clearinghouse*,
286 henceforth referred to as the clearinghouse, see Data and Resources Section) to enable data
287 sharing between members. This was accessible only to members of the SAG, allowing model
288 results to be independently reviewed and discussed before being shared openly with relevant
289 stakeholders and the public. While delaying the public distribution of model results, this allowed
290 crucial discussions on the model’s potential accuracy and utility, which was felt necessary due to
291 this being the first event the model had been applied to in near real-time. It also facilitated
292 discussions as to which stakeholders would benefit most from the model outputs. A more
293 detailed discussion of the distribution and utility of model results is provided below.

294 **RESULTS**

295 **Model 1: 0 days 21 hours 28 minutes post-earthquake**

296 Within a few hours of the earthquake occurring, consideration was given to whether manual
297 application of the model could produce results quickly enough to be of use in the response.
298 These discussions were hampered by the earthquake occurring on a Sunday in the UTC time
299 zone (Monday morning in NZST); however, approximately 18 hours after the earthquake
300 occurred, it was decided that manual application of the model could still be undertaken within a
301 useful timeframe. Manual downloading and processing of the necessary data sets began at
302 approximately 06:00 hrs on 14 November UTC, 0 days 18 hrs 58 mins after the earthquake
303 occurred. Priority was given to the largest datasets, namely the LINZ DEM and rivers database,
304 which required the longest downloading and processing times. Shaking data at this time were
305 sourced from the USGS ShakeMap® (see Data and Resources Section), which released initial
306 models < 10 mins after the earthquake based on GMPEs, and at the time was the only openly

307 available shaking data for the event. Data collection and processing were completed at 07:59 hrs
308 on 14 November UTC, 0 days 20 hrs 57 mins after the earthquake occurred. Model 1 (Fig. 4)
309 was subsequently completed and data provided to the SAG at 08:30 hrs on 14 November UTC, 0
310 days 21 hrs 28 mins after the earthquake occurred. Model 1 was therefore completed
311 approximately 2 hrs 30 mins after data collection and processing began, and just 31 mins after
312 this procedure was completed.

313 According to Model 1, the highest probability of landslides was concentrated in two
314 coastal areas immediately north and south of Kaikōura, where landslide likelihoods exceeded
315 80%. By this time several social media posts had reported landslides near to Kaikōura with
316 reports of blockages on SH1, but the full extent and intensity of landsliding was not yet known.
317 Landslide likelihoods > 60% (referred to as high risk i.e. those pixels where landslides were
318 more likely to occur than not) were modelled extending northwards from Waiau to Blenheim (~
319 130 km) and stretching inland from the coast for ~ 50 km to the slopes east of the Awatere
320 Valley Road, affecting a total area of ~ 6,500 km², suggesting that landsliding was expected to be
321 widespread.

322 Of the 1,832 road segments modelled, 560 (~ 30%) were identified as having at least one
323 danger pixel (i.e. with $\theta \geq 30^\circ$); the remaining 1,272 segments have no danger pixels and were
324 therefore considered to have no risk of landslide blockage. The most at-risk road segment was
325 located 20 km north of Kaikōura on SH1 at a location known as Ohau Point, where the risk of
326 blockage was 75%. In total, 46 segments of road were considered high risk (> 60%), of which 38
327 were on SH1 and three on the IKR. This immediately highlighted the possibility that Kaikōura
328 might be isolated with no road access possible. In addition, two segments on SH7 south of

329 Hanmer Springs were identified as high risk, along with three segments on the Awatere Valley
330 Road.

331 Out of the 8,456 river segments modelled, 5,089 were identified as having at least one
332 danger pixel, emphasising the high potential for landslide dam formation in this part of New
333 Zealand. In total, 241 river segments between Waiiau and Blenheim, and stretching inland as far
334 as the Awatere Valley Road, achieved high modelled risk values, suggesting that numerous
335 landslide dams were to be expected throughout this region. The highest likelihood was 79% and
336 occurred ~ 40km north-east of Kaikōura on the Clarence River. At the time, a landslide dam was
337 known to have occurred and subsequently failed at approximately 03:00 hrs on 14 November
338 UTC (Dellow et al., 2017), ~ 16 hrs after the earthquake and ~ 5 hrs 30 mins before Model 1 was
339 completed. While Model 1 was not completed in time to identify the Clarence River dam, this
340 provided confidence in the model's ability to produce useful results for other rivers.

341 **Model 2: 3 days 1 hour 28 minutes post-earthquake**

342 Following the completion of Model 1, we became aware that an alternative shaking model based
343 on local strong motion data sensors (see Horspool et al., 2015) had been released by GeoNet (see
344 Data and Resources Section), a collaboration between the New Zealand Earthquake Commission
345 and GNS Science that records information on New Zealand hazards. This data was downloaded
346 at 10:12 hrs on 16 November UTC, 2 days 23 hrs 10 mins after the earthquake; however, these
347 data were available at least as early as 22:06 hrs on 15 November UTC. Consequently, a second
348 round of landslide modelling based on this data was undertaken. Model 2 (Fig. 5) was completed
349 and shared with the SAG at 12:30 hrs on 16 November UTC, 3 days 1 hr 28 mins after the
350 earthquake occurred. Combining these results with Model 1 at the time allowed the authors and

351 the SAG to qualitatively evaluate the level of (un)certainty to place on the outputs, allowing
352 varying degrees of confidence to be placed on the resulting conclusions.

353 In total, 60% of pixels, accounting for an area $\sim 19,000 \text{ km}^2$, were unchanged in terms of
354 landslide hazard between Model 1 and Model 2. A total of 17% of pixels ($\sim 5,500 \text{ km}^2$) increased
355 in hazard, although of these, 75% increased by $\leq 10\%$, a change that was considered negligible.
356 Significant hazard increases therefore occurred in just 4% of pixels (220 km^2), the majority of
357 which were located on the eastern-most slopes between Kaikōura and Ward, but some of which
358 were on slopes south of Waiiau (Fig. 5). However, there were also significant hazard decreases
359 (changes $> 10\%$) on slopes east of the Awatere Valley Road. Consequently, high landslide
360 hazard values ($> 60\%$) in Model 2 extended north-east along the coast for $\sim 170 \text{ km}$ and inland
361 for $\sim 40 \text{ km}$, affecting a total area of $\sim 6,800 \text{ km}^2$, which is slightly larger than Model 1. The
362 maximum modelled landslide hazard increased from 85% to 89% but remained in the same area
363 as Model 1, on the slopes immediately north of Kaikōura (Fig. 5b).

364 Notwithstanding the slight increase in some landslide hazard values in Model 2, there
365 was little overall change in the total modelled risk of road blockages. In total, risk values
366 increased for 44 road segments, with an average increase of 6%, and decreased for 37 segments,
367 with an average decrease of 7%. Notably, the highest risk of blockage on the network remained
368 on SH1 at Ohau Point, where it increased to 76%. The total number of road segments considered
369 high risk increased from 44 in Model 1 to 62 in Model 2, with 15 of these located on SH1 south
370 of Oaro and one each for SH7, the IKR, and the Awatere Valley Road. Despite this, there was a
371 notable decrease in risk values for several segments of SH1 north and south of Kaikōura, where
372 risk decreased from $\sim 65\%$ to $< 20\%$ (Fig. 5c).

373 Very little change in terms of landslide dam risk was observed between Model 1 and
374 Model 2, with 4,341 river segments (85% of the 5,089 at-risk segments) having scores that
375 differed by < 10% from Model 1. Of the 748 segments that changed by > 10%, 266 increased in
376 Model 2, 184 of which were located east of the Awatere Valley Road. The effect was to increase
377 the total number of river segments considered to be at high risk of blockage from 241 in Model 1
378 to 314 in Model 2. The majority of these changes occurred on rivers south of Waiau in the region
379 where landslide hazard also notably increased in Model 2 (Fig. 5b). The risk of landslide dams in
380 this region changed from 50-60% in Model 1 to 60-70% in Model 2. Consequently, Model 2
381 suggested that numerous landslide dams were expected to have occurred in this region,
382 something which Model 1 had not necessarily highlighted. The highest modelled risk was again
383 on the Clarence River, where risk increased marginally to 80%.

384 **MODEL VERIFICATION AND SENSITIVITY**

385 Quantitative analysis of the model's predictive ability in terms of landslide hazard, road blockage
386 risk, and landslide dam risk is undertaken by comparing the corresponding true and false positive
387 prediction rates. True positive rate, or hit rate, is the number of observed landslides (or
388 blockages) occurring in pixels predicted as a landslide as a percentage of the total number of
389 observed landslides. False positive rate, or false alarm rate, is the total number of pixels
390 predicting a landslide that have landslide non-occurrence as a percentage of the total number of
391 non-occurrence pixels. Because this requires the landslide hazard and risk results to take the
392 form of a binary prediction (i.e. landslide or no landslide; blocked or not blocked) rather than
393 continuous values, we set various threshold hazard and risk values in which pixels/segments
394 above the threshold predict landslide occurrence/blockage. We compute the number of hits and

395 false alarms for multiple hazard and risk thresholds taken at 0.01 intervals in order to test how
396 the predictions vary with increasing values of hazard and risk. Data on mapped landslides, road
397 blockages, and landslide dams is taken from a variety of publically available sources or through
398 the clearinghouse (see Data and Resources Section).

399 As well as the hit rate and false alarm rate, we calculate the relative true positive (RTP)
400 rate. This considers the proportion of hits as a proportion of all pixels predicting landslide
401 occurrence. A relative true positive rate of 75% therefore means three-quarters of all pixels
402 predicting landslides are hits, regardless of the absolute number of hits this represents. This
403 provides a measure of how much over-prediction is occurring in the model.

404 ***Landslide hazard models***

405 For landslide hazard (Figs 4b & 5b), we use a dataset of 10,454 landslide centroid points (Fig. 1)
406 mapped by GNS Science from satellite and aerial reconnaissance in the months following the
407 earthquake (Massey et al., This Issue). From this inventory, both models have a maximum hit
408 rate of 81% (Fig 6a), meaning that 19% of mapped landslides occurred in pixels where landslide
409 hazard = 0, i.e. slopes < 15°. This suggests this threshold may be too high for this event. The
410 maximum false alarm rate is similar for both models at a little over 50%. Importantly, the
411 number of false alarms decreases rapidly once hazard thresholds exceed 20% likelihood, while
412 the number of hits remains close to the maximum until hazard thresholds reach ~ 50%
413 likelihood. For thresholds > 50%, Model 2 notably achieves more hits than Model 1 for the same
414 threshold value (Fig. 6a); for high hazard pixels (likelihoods > 60%), Model 1 predicts 47% of
415 mapped landslides while Model 2 predicts 62%. This suggests that Model 2 forms the better
416 overall prediction, but that broadly both results are comparable.

417 Nevertheless, the RTP rates for both models are very low: Model 1 has a maximum RTP
418 rate of 9% while Model 2 has a maximum RTP rate of 22% (Fig. 6a). This means that both
419 models severely over-predict landslide hazard with ~ 80-90% of pixels where landslides were
420 predicted not experiencing a landslide. One reason for such low RTP rates is the large number of
421 non-occurrence pixels ($>10^7$). Thus a false alarm rate of 2-6% equates to a large number of
422 individual pixels compared to the number of observed landslides. However, it should be
423 highlighted that the landslide inventory used to calculate RTP rate is point source and therefore
424 each landslide is only represented by a single pixel. In reality, each landslide likely covers
425 multiple pixels which in the present analysis are considered non-occurrence pixels; Massey et al.
426 (This Issue) show that the mean landslide area is ~ 300 m², which equates to 12 pixels with a 25
427 m pixel size, while the largest was ~ 1,000,000 m², or 40,000 pixels. Consequently, the RTP
428 rates are minimum estimates and in reality, the model likely performs better than these values
429 suggest. Nevertheless, it is still likely that the results are over-predicted in terms of individual
430 pixels. This issue is common to most landslide hazard and susceptibility models and reflects the
431 difficulties associated with predicting landslide occurrence at such fine resolution.

432 ***Landslide road blockage risk models***

433 Road blockage risk predictions are tested using the 41 road blockages (Fig. 1) reported by the
434 New Zealand Transport Agency (NZTA). The approximate locations of many of these blockages
435 were known within a few days of the earthquake from a combination of aerial reconnaissance
436 and local reports. However, an official inventory with precise coordinates was not available on
437 the clearinghouse until > 1 week after the earthquake. Because risk was calculated for 1 km
438 segments of the road network, we compare observed blockages to the corresponding road
439 segment, and consequently some road segments may account for multiple observed blockages.

440 Model 1 achieves a maximum hit rate of 93% while Model 2 achieves 98%, with both
441 models achieving a maximum false alarm rate of 29% (Fig. 6b). However, there is a notable
442 disparity between the number of hits achieved as the risk values increase (Fig. 6b). Model 1 sees
443 no reduction in the number of hits until the risk threshold exceeds 53%, while Model 2 sees
444 decreases once the risk threshold exceeds 20%. For high risk segments, Model 1 successfully
445 predicts 71% of road blockages compared with Model 2 which predicts just 34%. Despite
446 differences in the decay in number of hits, both models have a similar decay in false alarms, with
447 virtually no false alarms registered in high risk segments.

448 Unlike with the raw hazard models, Model 1 is able to achieve high RTP rates,
449 suggesting the model works well as a predictive tool. A blockage risk threshold set at 60%
450 likelihood successfully predicts 70% (29 out of 41) of road blockages with an RTP rate of 66%,
451 which increases to 100% when the blockage risk threshold is increased to 68% likelihood (Fig.
452 6b). Comparatively, at a 60% blockage risk threshold, Model 2 achieves an RTP rate of just 23%
453 and accounts for just 34% of all observed blockages. Model 1 therefore not only forms the better
454 predictive model for road blockages, but it is useful for pinpointing the precise road segments
455 blocked by landslides with comparatively small over-prediction compared to the raw hazard
456 model. Nevertheless, the failure of Model 2 is surprising given it formed a marginally better
457 hazard prediction compared to Model 1.

458 ***Landslide dam risk models***

459 Landslide dam predictions are tested using a dataset of 58 landslide dams (Fig. 1) mapped by
460 GNS Science and others from aerial and ground-based reconnaissance, which was first publically
461 available from Environment Canterbury (see Data and Resources Section) on 1 December 2016
462 UTC (18 days after the earthquake). In total, Dellow et al. (2017) describe > 200 landslide dams

463 while the Environment Canterbury dataset contains 191; however, the majority of these are
464 located on order 1 and 2 rivers, which were not assessed in the near real-time modelling
465 campaign. Consequently, only the 58 landslide dams (30% of the total identified) located on
466 order 3 or larger rivers are used to quantitatively assess model performance. This suggests that
467 the modelling should have considered order 1 and 2 rivers as this is where the majority of
468 landslide dams formed and, in hindsight, river order is not directly attributable to consequent
469 landslide dam risk. As with road blockages, we compare observed landslide dams to the
470 corresponding river segment, and individual segments may therefore account for multiple
471 blockages.

472 Both models achieve maximum hit rates of 93%, with Model 2 accounting for 90% of
473 landslide dams in high blockage risk segments (Fig. 6c). However, both models have high
474 maximum false alarm rates, with Model 1 having 60% and Model 2 having 59%. Nevertheless, a
475 similar decay pattern is observed, with the number of false alarms decreasing for both models
476 when blockage risk thresholds exceed 15% while the number of hits remains constant until
477 blockage risk thresholds exceed 50%. Notably, Model 2 does not see hit rates decrease until
478 blockage risk thresholds exceed ~ 60% at which point the decay rate is similar to Model 1,
479 suggesting Model 2 is the better version.

480 RTP rates for landslide dam predictions are notably lower than achieved for road
481 blockage predictions and only marginally better than the low scores observed for the raw hazard
482 models. Model 1 achieves a maximum RTP rate of just 14%, while Model 2 achieves a
483 maximum of 29% (Fig. 6c). Again, this highlights that both models over-predict landslide dam
484 risk and, currently, may not be useful for pinpointing the exact locations of landslide dams. Part
485 of this issue may lie in the threshold reach angle used (30°) as in reality the total landslide

486 volume passing this threshold may be insufficient to dam a river. Nevertheless, the high hit rates
487 are encouraging, and if future iterations of the model can sustain such hit rates while reducing
488 the over-prediction, this model may form a useful tool for pinpointing landslide dam locations.

489 **Sensitivity analysis**

490 Using the output landslide hazard from Model 1, we now reassess the road blockage and
491 landslide dam risk using reach angle thresholds between 10° and 50° taken at 10° intervals, and
492 compare the number of hits and false alarms achieved with the results achieved during the
493 modelling campaign. The area between the true and false positive curves is calculated to find the
494 best performing model. For this analysis we use the outputs from Model 1 as this version
495 achieved comparable predictions for landslide dams and better predictions for road blockages
496 compared to Model 2.

497 For both road blockages and landslide dams, smaller reach angle thresholds are able to
498 achieve greater maximum hit rates (Fig. 7). The decay in hit rates with increasing risk values is
499 broadly equivalent for all thresholds however. Smaller threshold reach angles also achieve
500 greater false positive predictions (Fig. 7). The best performing threshold for road blockages is
501 found to be 30°, although the performance using 20° and 40° is comparable (Table 2). For
502 landslide dam risk, the 40° threshold achieves the greatest performance, although again the
503 performance of the 20° and 30° thresholds are comparable. We also calculated the RTP rates for
504 each of these thresholds, finding that for landslide dams the 40° threshold achieved a maximum
505 RTP rate of 25%, approximately double that of the 30° threshold (14%). Whilst still too low to
506 be useful for pinpointing landslide dams, this does suggest that if a similar increase were
507 observed for a 40° threshold in Model 2 (translating to a maximum RTP rate of ~60%), then this
508 version would begin to be useful for pinpointing landslide dams. This suggests that in future

509 applications of the model using a 40° reach angle threshold may be more appropriate for
510 landslide dam prediction, while retaining a 30° reach angle threshold for road blockages is
511 suitable. This likely relates to the landslide volume passing the corresponding reach angle;
512 comparatively little landslide debris is required to block traffic flow on roads compared to that
513 required to block river flow.

514 **DISCUSSION**

515 **Model 2 road blockage risk**

516 It is notable that Model 2 performs poorly at predicting road segments blocked by landslides,
517 despite performing marginally better than Model 1 at predicting landslide hazard and landslide
518 dam occurrence. The reason for this poor performance is Model 2's failure to successfully
519 predict 19 (46% of the total) road blockages on SH1 near to Kaikōura that were successfully
520 predicted by Model 1. Analysis of the mechanism causing this highlights that this failure resulted
521 from an error during the processing of the GeoNet shaking model during the near real-time
522 modelling campaign.

523 The GeoNet data does not provide offshore locations with *MMI* values (Fig. 5a). Shaking
524 data from GeoNet was downloaded as a gridded XML format, which contains point locations
525 with *MMI* values spaced at 1 km intervals; any points offshore are nominally assigned *MMI* = 1.
526 To convert a gridded point cloud into a raster file necessary for the landslide hazard modelling,
527 an inverse distance weighted interpolation was conducted. Consequently, where offshore grid
528 points were located close to the coastline, low *MMI* shaking was assigned to a small number of
529 onshore pixels (Fig. 8). This significantly reduced modelled landslide hazard in the
530 corresponding pixels and thus road blockage risk values for coastal segments of SH1. The small

531 total area affected by these anomalies explains why the landslide model remains comparable to
532 Model 1 in terms of overall landslide occurrence. Likewise, the lack of order 3+ rivers in these
533 locations explains why the model also remains comparable to Model 1 in terms of landslide dam
534 risk. Had offshore points been removed from the interpolation process at the time of the
535 modelling campaign, the resulting shaking raster would not have included anomalously low *MMI*
536 values onshore along the coast, resulting in the successful prediction of road blockages on
537 coastal SH1. Re-processing Model 2 using the corrected shaking data confirms this (Fig. 8). This
538 emphasises the importance of the initial input data and its handling, with errors and anomalies in
539 the data itself or in the data processing carrying through to final outputs, affecting the overall
540 model success.

541 **Implications for near real-time earthquake impact modelling**

542 We have shown that near real-time prediction of coseismic landsliding impacts can be
543 successfully and rapidly undertaken following a large earthquake. Currently, several near real-
544 time earthquake loss models exist, including the USGS Prompt Assessment of Global
545 Earthquakes for Response (PAGER; Jaiswal et al., 2011, 2009; Wald et al., 2008) and QLARM
546 (Trendafiloski et al., 2011); however, these models currently do not disaggregate losses by cause.
547 Coseismic landslides can account for large numbers of total earthquake fatalities (Yin et al.,
548 2009; Evans & Bent, 2004; Keefer, 1984) and are the primary cause of damage to linear
549 infrastructure such as transport and utilities networks during earthquakes (Bird & Bommer,
550 2004). Specifically identifying the impacts resulting from coseismic landslides is therefore
551 important for informing emergency response, as this may enable greater understanding of the
552 causes of impacts at different locations throughout the affected area.

553 This is particularly highlighted in the assessment of landslide dam risk. Because landslide
554 dams typically form in steep narrow catchments they are often difficult to identify from the
555 ground or from remotely sensed imagery, and so may go unnoticed in the immediate aftermath of
556 a large earthquake. The majority of landslide dams that fail do so soon after they form (Costa &
557 Schuster, 1988). Rapidly identifying the locations where landslide dams have formed is therefore
558 vital for post-earthquake response. However, current manual mapping techniques relying on
559 optical aerial and/or satellite reconnaissance are unsuitable for such a task because they can be
560 slow and weather dependent. Initial, incomplete landslide inventories identified from satellite
561 imagery only became available > 5 days after the Kaikōura earthquake had occurred (Sotiris et
562 al., 2016). However, this initial inventory contained < 10% of the total landslides mapped by
563 Massey et al. (This Issue), while an updated inventory released > 12 days after the earthquake
564 still only contained ~ 50%. Further, identification of landslide dams was not completed until 18
565 days after the earthquake. In contrast, Model 1 was successfully completed < 24 hours after the
566 earthquake, with Model 2 available ~ 72 hours after the earthquake. Effective near real-time
567 modelling of landsliding and associated losses can clearly provide a faster assessment of post-
568 earthquake risk from hazards such as landslide dams. Using these outputs to prioritise locations
569 for aerial and satellite reconnaissance is therefore likely to provide a better approach to rapidly
570 identifying coseismic landslide impacts.

571 **Model use in response to the Kaikōura earthquake**

572 Upon completion, the near real-time model outputs (Figs. 4 & 5) were shared with the
573 earthquake response SAG and uploaded to the clearinghouse. The SAG met regularly during the
574 response via video conference to discuss the evolving situation and consider new information as
575 it became available. The landslide model outputs were initially uploaded to the clearinghouse for

576 discussion within the SAG to formulate a useful and consistent interpretation of the results that
577 could be shared with relevant stakeholders.

578 At the time, the model outputs proved useful in two primary ways. Firstly, Model 1
579 results were shared with the NZTA on 15 November UTC in order to help inform their strategy
580 meeting that day. Of particular interest was the landslide dam risk as, > 48 hours after the
581 earthquake, the road functionality was generally known to NZTA. However, NZTA remained
582 concerned about the threat of outburst floods to key bridges as well as to engineering teams
583 tasked with attempting to reinstate the roads. A further concern was identifying how many
584 people were inaccessible by road and at risk of outburst flood in order to inform decisions of
585 potential emergency evacuation.

586 Secondly, several members of the SAG were involved in aerial reconnaissance of the
587 affected area, with a particular focus on identifying and monitoring landslide dams. The results
588 of both Model 1 and Model 2 were therefore used to prioritise flight paths over the affected
589 region. As a result, reconnaissance flights between 15 and 23 November undertook flight paths
590 that focussed on the small catchments between the epicentral region and the hills immediately
591 north of Kaikōura, where the majority of landslide dams were predicted and later identified.
592 While this area was considered high priority prior to the model results becoming available, the
593 models did enable more detailed prioritisation of individual catchments.

594 **Future automation**

595 Once a decision to manually apply the coseismic landslide impact model had been taken, the
596 majority of the time required to produce the initial model outputs comprised downloading and
597 processing the required data. This time could be substantially reduced by creating a standing
598 repository of the necessary model data. The only input data not available pre-earthquake are the

599 resulting shaking data and thus the majority of the data can be acquired and consequent
600 calculations undertaken before an earthquake occurs (Fig. 2). Manual application of the model
601 took ~ 31 mins from the completion of data download and preparation. With initial shaking data
602 available from the USGS < 10 mins after an earthquake, Model 1 predictions could therefore
603 have been available within 45 mins of the Kaikōura earthquake occurring, under ideal
604 circumstances.

605 Ideally, this time could further be reduced by automating the method so that manual
606 intervention is not required. This would allow the model to produce results consistently
607 regardless of time of day, week, or year. The relative simplicity of the approach and underlying
608 calculations makes automation of this method a simple task, especially since most of the
609 calculations can be undertaken *a priori*. Furthermore, presently, the model violates a primary
610 condition of near real-time modelling systems in that it is reliant on external calculations of
611 shaking intensity. The model therefore needs to be adapted to be entirely independent by
612 incorporating its own internal shaking intensity estimates. Alternatively, specifically developing
613 the method as an add-on to current near real-time shaking predictions, such as the USGS
614 ShakeMap or PAGER, would allow it to use the resulting shake maps directly, effectively
615 incorporating it into these existing near real-time models and further reducing the time required.
616 Under such conditions, landslide impact predictions could be completed within 10-15 mins of the
617 earthquake occurring, at the same time as the first shaking models become available.

618 **Limitations and uncertainties**

619 Despite the modelling presented having been shown to be useful for a post-earthquake
620 emergency response, there are important limitations to consider. Most importantly, the landslide
621 hazard models (Figs. 4b and 5b), and to a lesser degree the landslide dam models (Figs. 4d and

622 5d), are significantly over-predicted. This is a major limitation of the model and makes the
623 output, in its current form, ineffective at pinpointing the precise locations of landslides caused by
624 the earthquake. However, as highlighted above, these RTP rates are likely minimum values due
625 to the landslide inventory used in verification comprising point sources rather than polygons.
626 Reassessing the RTP rates when polygon source become available will allow the true RTP rate to
627 be calculated allowing a fairer estimation of the true over-prediction. Nevertheless, the model
628 outputs are still expected to be over-predicted and this must be addressed in future iterations if
629 this technique is to prove useful in an emergency response.

630 The models outputs do not presently take the form of a binary prediction of landslide
631 occurrence, but instead are presented as a continuous scale of landslide hazard or risk (i.e.
632 relative likelihood of landslide occurrence). While such a continuous output may have some
633 benefits, the outputs would arguably be enhanced for response purposes by converting to a direct
634 prediction of where landslides have occurred. The limitation here is determining which threshold
635 value to set in order to form a binary prediction, which is ultimately subjective, and the utility to
636 end-users of true probability values. A recent attempt has been made to model landslide hazard
637 in terms of true probability, using observations from relatively large numbers of global
638 earthquakes (Parker et al., 2017). While this approach has been shown to yield consistently
639 accurate predictions of landslide probability from test earthquakes, it has yet to be applied in
640 (near) real-time following an earthquake.

641 The model outputs provide no information on the potential size, mechanism, or
642 consequent damage of the landslides triggered. At a local scale, the total volume and area
643 involved in a landslide, as well as the mechanism and style of motion, are vital indicators of the
644 hazard posed, and the potential damage. Vulnerability of roads to landslide losses is also a

645 critical component of risk. Currently the model only assesses the likelihood of landslides
646 reaching the road network, not the damage that they cause. Similarly, for landslide dams, the
647 model currently only predicts the likelihood of a landslide reaching the river; it does not consider
648 the potential for the landslide to subsequently block the river, which may further explain the
649 over-prediction in this component of the model. Finding ways to incorporate such information
650 into future models could therefore improve the overall usefulness and further reduce over-
651 prediction.

652 Finally, this is the only time that this method has been attempted during a live earthquake
653 response. Whilst the results are encouraging, particularly for road blockage prediction, and the
654 use of the outputs highlights the need for and value of such models, it is not guaranteed that
655 applying the same model to future earthquakes elsewhere will produce similarly successful
656 results. Consequently, further testing of the method on historic earthquakes is required before it
657 can be more widely operationalised. Despite this, the underlying hazard model of Kritikos et al.
658 (2015) has now been shown to be successful for three different earthquakes in New Zealand, and
659 thus New Zealand seems likely to prove a suitable site for continued testing and initial
660 implementation of this near real-time modelling approach.

661 **CONCLUSIONS**

662 Following the 13 November 2016 UTC Kaikōura earthquake in New Zealand, we undertook a
663 near real-time landslide hazard and impact modelling campaign in an attempt to provide critical
664 information for emergency responders. The landslide hazard model used an empirical approach
665 using fuzzy logic in GIS based on global observations of the relationships between landslide
666 occurrence and predisposing factors. The impact models used a simplified analysis of landslide

667 mobility based on reach angles to identify pixels from which any landslide posed a risk to nearby
668 roads and rivers. The model did not account for vulnerability of roads and rivers to landslide
669 blockage, instead focussing simply on locations where landslides could intersect the feature. The
670 approach was undertaken manually following the earthquake and therefore its capabilities as an
671 automatic system have not been properly tested.

672 The outputs from these models accurately accounted for the majority of landslides, road
673 blockages and landslide dams that formed during the earthquake. Importantly, the first models,
674 based on initial shaking outputs from the USGS, were available just 21 hrs 28 mins after the
675 earthquake, > 4 days before the first, incomplete assessment of landsliding from traditional
676 mapping efforts. A second iteration of the model based on updated shaking outputs was available
677 ~72 hrs after the earthquake and generally performed better than the initial model. While both
678 models accurately accounted for the majority of landslides and landslide dams, it is notable that
679 these models were especially over-predicted, and therefore require continued refinement to the
680 modelling methods to reduce this over-prediction. Nevertheless, the model was able to perform
681 well in identifying road blockages, with limited over-prediction observed suggesting this
682 approach may prove useful at accurately predicting road impacts from landslides in future
683 earthquakes.

684 While the present results are promising, continued efforts to streamline and automate the
685 modelling methods is required. An automated version of the model may be able to produce
686 future outputs within 10-15 mins of an earthquake occurring, significantly improving the times
687 achieved in this study through manual application. Incorporating the vulnerability of roads and
688 rivers into the model is a further aim, as this is a crucial component of any disaster management
689 system as its assessment can be used as an input for decision making during an emergency

690 response. Finally, efforts to improve the model in order to reduce the over-prediction associated
691 with the landslide hazard and landslide dam risk outputs is essential if future iterations are to be
692 useful for pinpointing the precise locations of landslides and landslide dams.

693 **DATA & RESOURCES**

694 Landslide and road blockage data used in this study were collected from the private *Engineering*
695 *Response to the M7.8 Kaikoura earthquake clearinghouse* set up for secure data sharing post-
696 earthquake and is not available to the public. The landslide inventory used in this study to assess
697 model performance was kindly supplied to the authors by Chris Massey of GNS Science and is
698 described in Massey et al (This Issue). Publically available data on landslide locations is
699 available from Sotiris et al. (2016) and can be obtained from
700 <https://zenodo.org/record/167130#.WZRwt1WGNhG> (last accessed August 2017). Landslide
701 dam locations were taken from the Environment Canterbury website and can be accessed at
702 [http://ecan.maps.arcgis.com/apps/Cascade/index.html?appid=50f00d42e29c46b1a61b848440c52](http://ecan.maps.arcgis.com/apps/Cascade/index.html?appid=50f00d42e29c46b1a61b848440c5295a)
703 [95a](#) (last accessed August 2017). Shaking data was downloaded at the time from the USGS and
704 GeoNet, and is available from
705 <https://earthquake.usgs.gov/earthquakes/eventpage/us1000778i#executive> (last accessed
706 November 2016) and <http://shakemap.geonet.org.nz/data/2016p858000/output/grid.xml> (last
707 accessed Novemeber 2016). All other data in this paper came from published sources listed in
708 the references.

709 **ACKNOWLEDGEMENTS**

710 The authors would like to thank the members of the New Zealand earthquake response SAG who
711 used the outputs of this study at the time and subsequently helped to improve both the model
712 outputs and this manuscript. In particular we thank Liam Wotherspoon for his helpful thoughts
713 and comments which helped improve the manuscript from its original draft, and Chris Massey for
714 providing access to the GNS Science landslide inventory. We thank the two anonymous reviewers
715 whose comments helped improve this manuscript. This study was supported by the DIFeREns2
716 (2014-2019) COFUND scheme supported by the European Union's Seventh Framework
717 Programme (grant number 609412).

718 **REFERENCES**

- 719 Bannister, S. & Gledhill, K. (2012). Evolution of the 2010-2012 Canterbury earthquake sequence.
720 *New Zealand Journal of Geology and Geophysics*. 55 (3). p.pp. 295–304.
- 721 Bird, J.F. & Bommer, J.J. (2004). Earthquake losses due to ground failure. *Engineering Geology*.
722 75 (2). p.pp. 147–179.
- 723 Borella, J.W., Quigley, M. & Vick, L. (2016). Anthropocene rockfalls travel farther than
724 prehistoric predecessors. *Science Advances*. 2 (9).
- 725 Bui, D.T., Pradhan, B., Lofman, O., Revhaug, I. & Dick, O.B. (2012). Spatial prediction of
726 landslide hazards in Hoa Binh province (Vietnam): A comparative assessment of the efficacy
727 of evidential belief functions and fuzzy logic models. *CATENA*. 96. p.pp. 28–40.
- 728 Costa, J.E. & Schuster, R.L. (1988). The formation and failure of natural dams. *Geological Society
729 of America Bulletin*. 100. p.pp. 1054–1068.
- 730 Davies, A.J., Sadashiva, V., Aghababaei, M., Barnhill, D., Costello, S.B., Fanslow, B., Headifen,

731 D., Hughes, M., Kotze, R., Mackie, J., Ranjitkar, P., Thompson, J., Troitino, D.R., Wilson,
732 T., Woods, S. & Wotherspoon, L.M. (2017). Transport infrastructure performance and
733 management in the South Island of New Zealand, during the first 100 days following the 2016
734 Mw 7.8 Kaikōura earthquake. *Bulletin of the New Zealand Society for Earthquake*
735 *Engineering*. 50 (2).

736 Davies, T.R., McSaveney, M.J. & Hodgson, K.A. (1999). A fragmentation-spreading model for
737 long-runout rock avalanches. *Canadian Geotechnical Journal*. 36 (6). p.pp. 1096–1110.

738 Dellow, S., Massey, C., Cox, S., Archibald, G., Begg, J., Bruce, Z., Carey, J., Davidson, J., Pasqua,
739 F. Della, Glassey, P., Hill, M., Jones, K., Lyndsell, B., Lukovic, B., Mccoll, S., Rattenbury,
740 M., Read, S., Rosser, B., Singeisen, C., Townsend, D., Villamor, P., Villeneuve, M.,
741 Wartman, J., Rathje, E., Sitar, N., Adda, A.-Z., Manousakis, J. & Little, M. (2017). Landslides
742 caused by the Mw7.8 Kaikōura earthquake and the immediate response. *Bulletin of the New*
743 *Zealand Society for Earthquake Engineering*. 50 (2).

744 Evans, S.G. & Bent, A.L. (2004). The Las Colinas landslide, Santa Tecla - A highly destructive
745 flowslide triggered by the January 13, 2001, El Salvador earthquake. In: W. I. Rose, J. J.
746 Bommer, D. L. Lopez, M. J. Carr, & J. J. Major (eds.). *Natural Hazards in El Salvador:*
747 *Geological Society of America Special Paper 375*. pp. 25–38.

748 Gallen, S.F., Clark, M.K., Godt, J.W., Roback, K. & Niemi, N.A. (2016). Application and
749 evaluation of a rapid response earthquake-triggered landslide model to the 25 April 2015 Mw
750 7.8 Gorkha earthquake, Nepal. *Tectonophysics*.

751 Giovinazzi, S., Wilson, T., Davis, C., Bristow, D., Gallagher, M., Schofield, A., Villemure, M.,
752 Eiding, J. & Tang, A. (2011). Lifelines performance and management following the 22
753 February 2011 Christchurch earthquake, New Zealand: Highlights of resilience. *Bulletin of*

754 *the New Zealand Society for Earthquake Engineering*. 44 (4). p.pp. 402–417.

755 Godt, J.W., Baum, R.L., Savage, W.Z., Salciarini, D., Schulz, W. & Harp, E.L. (2008). Transient
756 deterministic shallow landslide modelling: requirements for susceptibility and hazard
757 assessments in a GIS framework. *Engineering Geology*. 102. p.pp. 214–226.

758 Hamling, I.J., Hreinsdóttir, S., Clark, K., Elliott, J., Liang, C., Fielding, E., Litchfield, N.,
759 Villamor, P., Wallace, L., Wright, T.J., D’Anastasio, E., Bannister, S., Burbidge, D., Denys,
760 P., Gentle, P., Howarth, J., Mueller, C., Palmer, N., Pearson, C., Power, W., Barnes, P.,
761 Barrell, D.J.A., Van Dissen, R., Langridge, R., Little, T., Nicol, A., Pettinga, J., Rowland, J.
762 & Stirling, M. (2017). Complex multifault rupture during the 2016 Mw 7.8 Kaikōura
763 earthquake, New Zealand. *Science*. eaam7194.

764 Horspool, N.A., Chadwick, M., Ristau, J., Salichon, J. & Gerstenberger, M.C. (2015).
765 ShakeMapNZ: Informing post-event decision making. *Proceedings of the New Zealand*
766 *Society for Earthquake Engineering Conference*.

767 Hsü, K.J. (1975). Catastrophic Debris Streams (Sturzstroms) Generated by Rockfalls. *Geological*
768 *Society of America Bulletin*. 86. p.pp. 129–140.

769 Hungr, O. (1995). A model for the runout analysis of rapid flow slides, debris flows, and
770 avalanches. *Canadian Geotechnical Journal*. 32 (4). p.pp. 610–623.

771 Hungr, O. (2006). Rock avalanche occurrence, process and modelling. In: *Landslides from*
772 *Massive Rock Slope Failure*. Dordrecht: Springer Netherlands, pp. 243–266.

773 Jaiswal, K., Wald, D.J., Earle, P.S., Porter, K.A. & Hearne, M. (2011). Earthquake Casualty
774 Models Within the USGS Prompt Assessment of Global Earthquakes for Response (PAGER)
775 System. In: R. Spence (ed.). *Human Casualties in Earthquakes*. Advances in Natural and
776 Technological Hazards Research. 2011.

777 Jaiswal, K., Wald, D.J. & Hearne, M. (2009). *Estimating Casualties for Large Earthquakes*
778 *Worldwide Using an Empirical Approach*.

779 Jibson, R.W., Harp, E.L. & Michael, J.A. (2000). A method for producing digital probabilistic
780 seismic landslide hazard maps. *Engineering Geology*. 58. p.pp. 271–289.

781 Kaiser, A., Balfour, N., Fry, B., Holden, C., Litchfield, N., Gerstenberger, M., D’Anastasio, E.,
782 Horspool, N., McVerry, G., Ristau, J., Bannister, S., Christophersen, A., Clark, K., Power,
783 W., Rhoades, D., Massey, C., Hamling, I., Wallace, L., Mountjoy, J., Kaneko, Y., Benites,
784 R., Van Houtte, C., Dellow, S., Wotherspoon, L., Elwood, K. & Gledhill, K. (2017). The
785 2016 Kaikōura, New Zealand, Earthquake: Preliminary Seismological Report. *Seismological*
786 *Research Letters*. 88 (3).

787 Kanungo, D.P., Arora, M.K., Gupta, R.P. & Sarkar, S. (2008). Landslide risk assessment using
788 concepts of danger pixels and fuzzy set theory in Darjeeling Himalayas. *Landslides*. 5 (4).
789 p.pp. 407–416.

790 Keefer, D.K. (1984). Landslides caused by earthquakes. *Geological Society of America Bulletin*.
791 95. p.pp. 406–421.

792 Kritikos, T. & Davies, T. (2015). Assessment of rainfall-generated shallow landslide/debris-flow
793 susceptibility and runout using a GIS-based approach: application to western Southern Alps
794 of New Zealand. *Landslides*. 12 (6). p.pp. 1051–1075.

795 Kritikos, T., Robinson, T.R. & Davies, T.R.H. (2015). Regional coseismic landslide hazard
796 assessment without historical landslide inventories: A new approach. *Journal of Geophysical*
797 *Research : Earth Surface*. 120. p.pp. 1–19.

798 Legros, F. (2002). The mobility of long-runout landslides. *Engineering Geology*. 63 (3–4). p.pp.
799 301–331.

800 Marc, O., Hovius, N. & Meunier, P. (2016). The mass balance of earthquakes and earthquake
801 sequences. *Geophysical Research Letters*. 43 (8). p.pp. 3708–3716.

802 Meinhardt, M., Fink, M. & Tünschel, H. (2015). Landslide susceptibility analysis in central
803 Vietnam based on an incomplete landslide inventory: Comparison of a new method to
804 calculate weighting factors by means of bivariate statistics. *Geomorphology*. 234. p.pp. 80–
805 97.

806 Newmark, N.M. (1965). Effects of earthquakes on dams and embankments. *Milestones in Soil*
807 *Mechanics*.

808 Nowicki, M.A., Wald, D.J., Hamburger, M.W., Hearne, M. & Thompson, E.M. (2014).
809 Development of a globally applicable model for near real-time prediction of seismically
810 induced landslides. *Engineering Geology*. 173. p.pp. 54–65.

811 Parker, R.N., Rosser, N.J. & Hales, T.C. (2017). Spatial prediction of earthquake-induced landslide
812 probability. *Natural Hazards and Earth System Sciences Discussions*.

813 Paterson, B.R. & Bourne-Webb, P.J. (1994). Reconnaissance report on highway damage from the
814 18 June 1994, Arthurs Pass earthquake. *Bulletin of the New Zealand Society for Earthquake*
815 *Engineering*. 27 (3). p.pp. 222–226.

816 Pellicani, R., Van Westen, C.J. & Spilotro, G. (2014). Assessing landslide exposure in areas with
817 limited landslide information. *Landslides*. 11 (3). p.pp. 463–480.

818 Pourghasemi, H.R., Pradhan, B. & Gokceoglu, C. (2012). Application of fuzzy logic and analytical
819 hierarchy process (AHP) to landslide susceptibility mapping at Haraz watershed, Iran.
820 *Natural Hazards*. 63 (2). p.pp. 965–996.

821 Power, W., Downes, G., McSaveney, M., Beavan, J. & Hancox, G.T. (2005). The Fiordland
822 earthquake and tsunami, New Zealand, 21 August 2003. In: K. Satake (ed.). *Tsunamis: Case*

823 *Studies and Recent Developments*. 2005, pp. 31–42.

824 Pradhan, B. (2010). Landslide susceptibility mapping of a catchment area using frequency ratio,
825 fuzzy logic and multivariate logistic regression approaches. *Journal of the Indian Society of*
826 *Remote Sensing*. 38 (2). p.pp. 301–320.

827 Robinson, T.R., Buxton, R., Wilson, T.M., Cousins, J. & Christophersen, A. (2015). *Multiple*
828 *infrastructure failures and restoration estimates from an Alpine Fault earthquake: Capturing*
829 *modelling information for MERIT*.

830 Robinson, T.R., Davies, T.R.H., Wilson, T.M. & Orchiston, C. (2016a). Coseismic landsliding
831 estimates for an Alpine Fault earthquake and the consequences for erosion of the Southern
832 Alps, New Zealand. *Geomorphology*. 263. p.pp. 71–86.

833 Robinson, T.R., Davies, T.R.H., Wilson, T.M., Orchiston, C. & Barth, N. (2016b). Evaluation of
834 coseismic landslide hazard on the proposed Haast-Hollyford Highway, South Island, New
835 Zealand. *Georisk: Assessment and Management of Risk for Engineered Systems and*
836 *Geohazards*. 10 (2).

837 Robinson, T.R., Rosser, N.J., Densmore, A.L., Williams, J.G., Kincey, M.E., Benjamin, J. & Bell,
838 H.J.A. (2017). Rapid post-earthquake modelling of coseismic landslide magnitude and
839 distribution for emergency response decision support. *Natural Hazards and Earth Systems*
840 *Sciences*.

841 Sotiris, V., George, P. & Spyros, P. (2016). *Preliminary Map of Co-Seismic Landslides for the M*
842 *7.8 Kaikoura, New Zealand Earthquake [Data Set]*. 2016. Zenodo.

843 Stirling, M.W., Litchfield, N.J., Villamor, P., Van Dissen, R.J., Nicol, A., Pettinga, J., Barnes, P.,
844 Langridge, R.M., Little, T., Barrell, D.J.A., Mountjoy, J., Ries, W.F., Rowland, J., Fenton,
845 C., Hamling, I., Asher, C., Barrier, A., Benson, A., Bischoff, A., Borella, J., Carne, R.,

846 Cochran, U.A., Cockroft, M., Cox, S.C., Duke, G., Fenton, F., Gasston, C., Grimshaw, C.,
847 Hale, D., Hall, B., Hao, K.X., Hatem, A., Hemphill-Haley, M., Heron, D.W., Howarth, J.,
848 Juniper, Z., Kane, T., Kears, J., Khajavi, N., Lamarche, G., Lawson, S., Lukovic, B.,
849 Madugo, C., Mccoll, S., Noble, D., Pedley, K., Sauer, K., Stahl, T., Strong, D.T., Townsend,
850 D.B., Toy, V., Villeneuve, M., Wandres, A., Williams, J., Woelz, S. & Zinke, R. (2017). The
851 Mw 7.8 2016 Kaikōura earthquake: surface fault rupture and seismic hazard context. *Bulletin*
852 *of the New Zealand Society for Earthquake Engineering*. 50 (2).

853 Trendafiloski, G., Wyss, M. & Rosset, P. (2011). Loss Estimation Module in the Second
854 Generation Software QLARM. In: R. Spence (ed.). *Human Casualties in Earthquakes*.
855 Advances in Natural and Technological Hazards Research. 2011.

856 Wadge, G., Francis, P.W. & Ramirez, C.F. (1995). The Socompa collapse and avalanche event.
857 *Journal of Volcanology and Geothermal Research*. 66. p.pp. 309–336.

858 Wald, D., Lin, K.-W., Porter, K. & Turner, L. (2008). ShakeCast: Automating and Improving the
859 Use of ShakeMap for Post-Earthquake Decision-Making and Response. *Earthquake Spectra*.
860 24 (2). p.pp. 533–553.

861 Williams, J.G., Rosser, N.J., Kinsey, M.E., Benjamin, J., Oven, K.J., Densmore, A.L., Milledge,
862 D.G. & Robinson, T.R. (2017). Satellite-based emergency mapping: Landslides triggered by
863 the 2015 Nepal earthquake. *Natural Hazards and Earth System Sciences Discussion*.

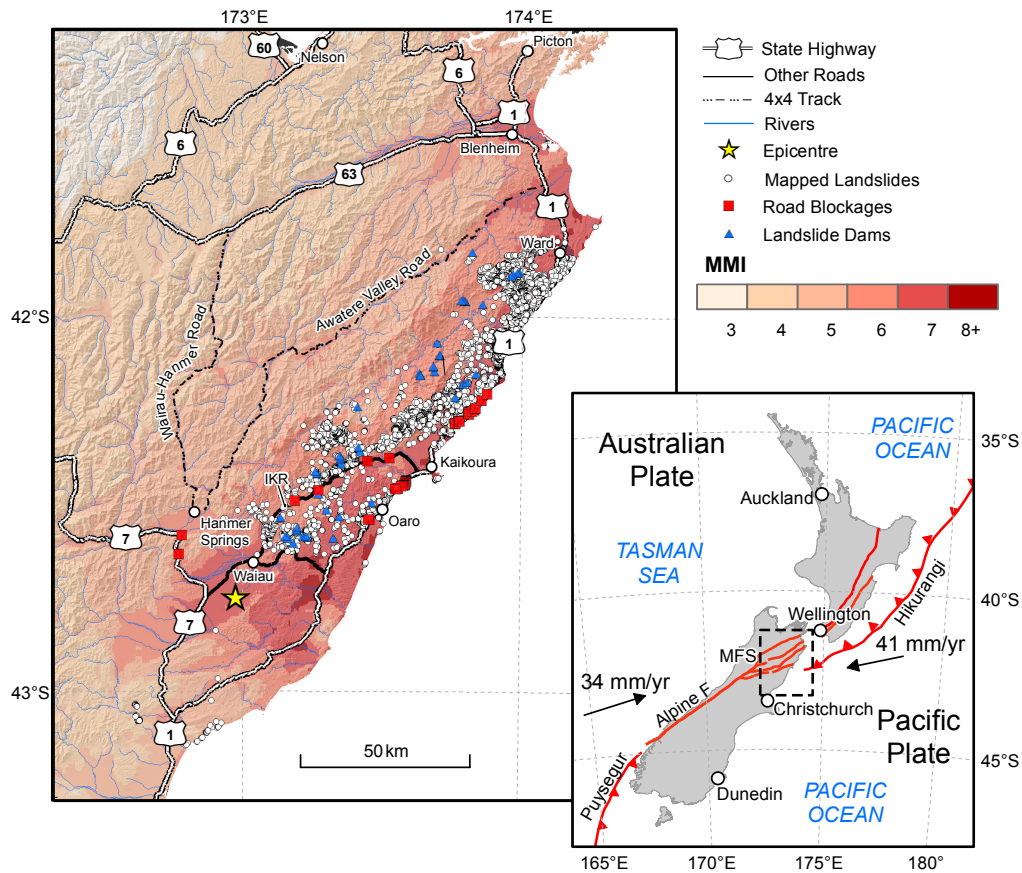
864 Woods, R.J., McBride, S.K., Wotherspoon, L.M., Beaven, S., Potter, S.H., Johnston, D.M.,
865 Wilson, T.M., Brunson, D., Grace, E.S. & Brackley, H. (2017). Science to Emergency
866 Management Response: Kaikoura Earthquakes 2016. *Bulletin of the New Zealand Society for*
867 *Earthquake Engineering*. 50 (2). p.pp. 329–337.

868 Yin, Y., Wang, F. & Sun, P. (2009). Landslide hazards triggered by the 2008 Wenchuan

869 earthquake, Sichuan, China. *Landslides*. 6 (2). p.pp. 139–152.

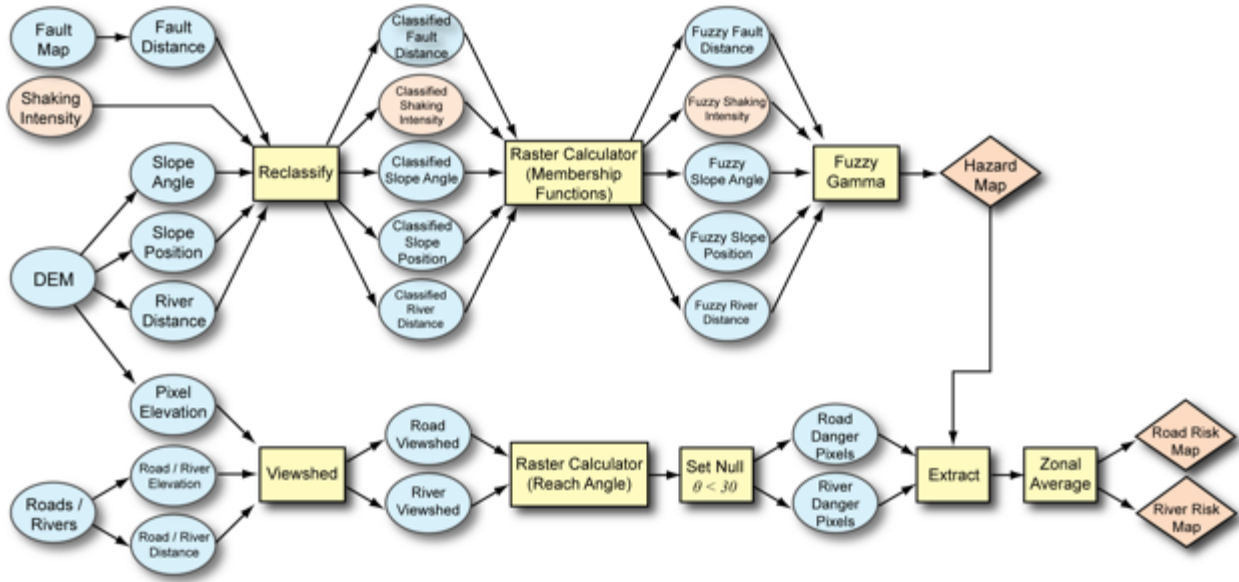
870

871 LIST OF FIGURES:



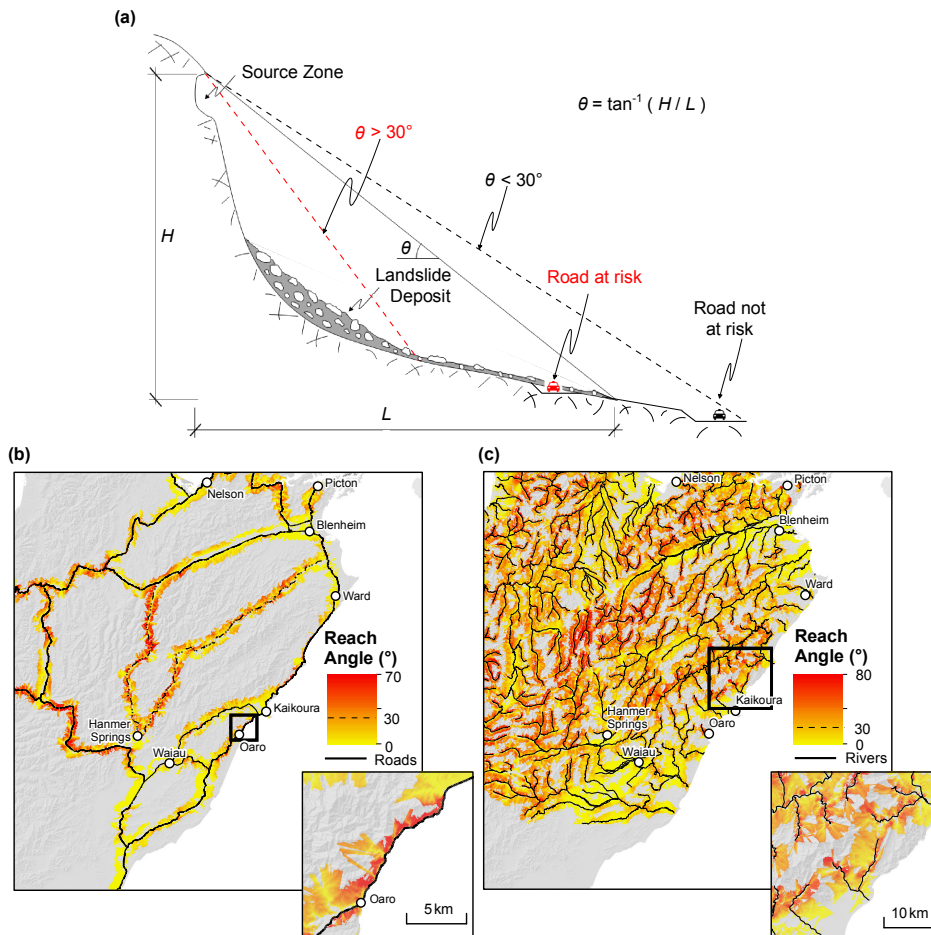
872

873 Figure 1: Ground shaking and observed landslides from the M_w 7.8 Kaikōura earthquake in
 874 relation to critical transport infrastructure and rivers. Shaking data from GeoNet downloaded at
 875 10:12 hrs on 16 November 2016 UTC (+2 days 23 hrs 10 mins). Landslides mapped by Massey
 876 et al. (This Issue). Landslide road blockages reported by the New Zealand Transport Agency and
 877 downloaded from the clearinghouse > 1 week after the event. Landslide dams located by ECan
 878 (2017a) based on aerial reconnaissance and publically released on 1 December 2016 UTC (+18
 879 days). Inset: Tectonic setting of New Zealand showing major faults associated with the
 880 Australia-Pacific plate boundary. MFS – Marlborough Fault System; Alpine F – Alpine Fault;
 881 IKR – Inland Kaikōura Road.



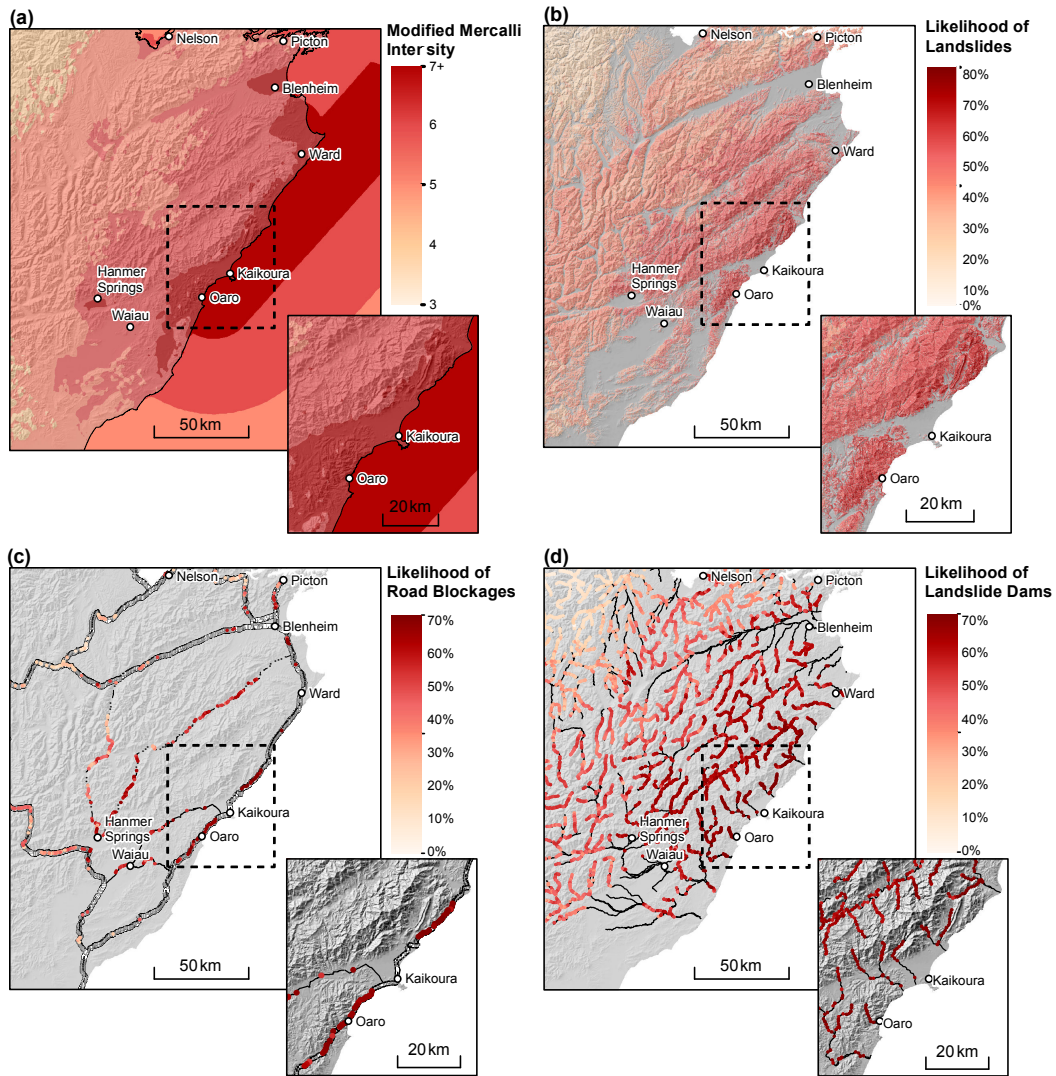
882

883 Figure 2: Simplified workflow for near real-time landslide hazard and risk modelling. Circles
 884 represent input or derived data; squares represent model processes; diamonds represent key
 885 model outputs. All data except shaking intensity and its consequent derived data is available pre-
 886 earthquake.



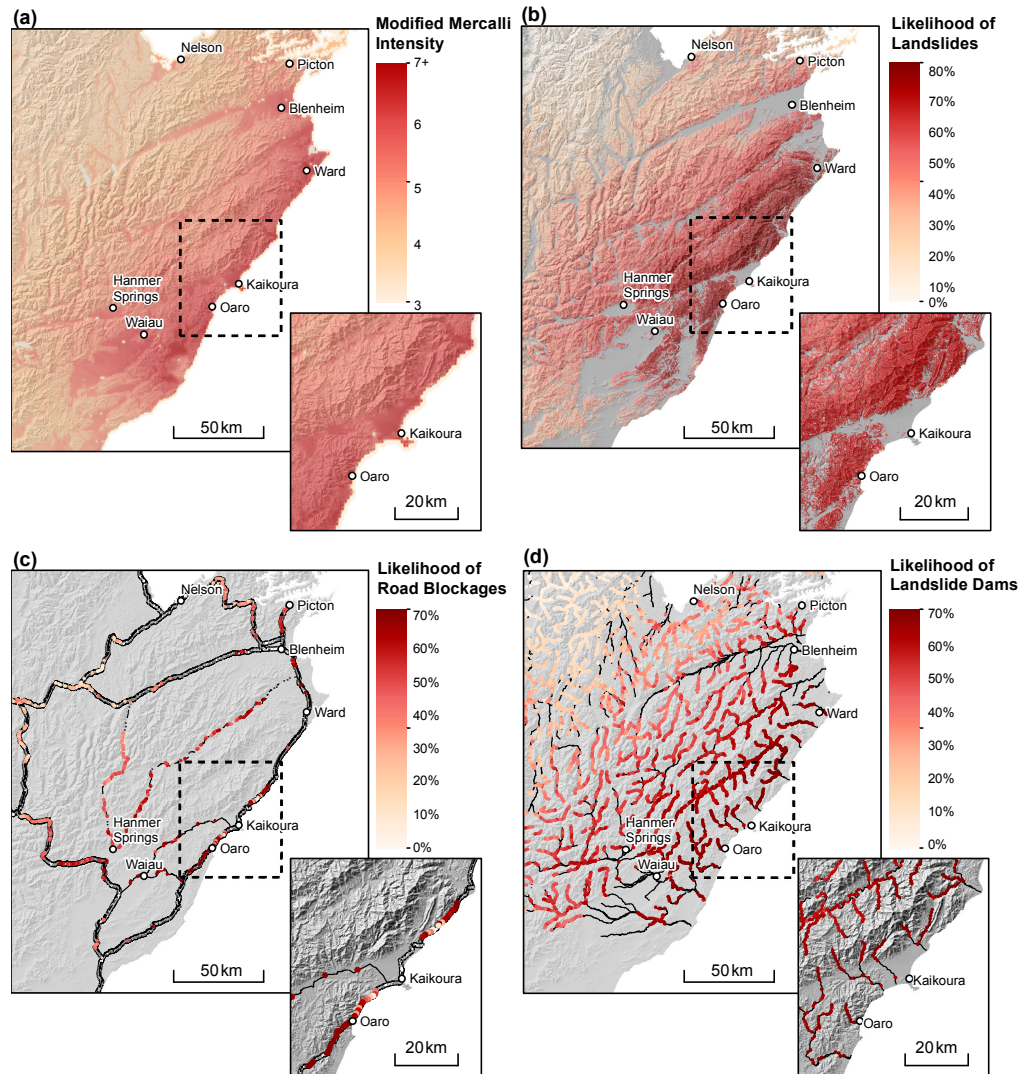
887

888 Figure 3: Landslide reach angle and danger pixels for the South Island State Highway and order
 889 3+ river networks. (a) Landslide runout concepts, adapted from Hungr et al. (2005). H – vertical
 890 drop; L – horizontal distance; θ – reach angle. Pixels with reach angles $> 30^\circ$ are considered to be
 891 at risk from landslide blockages, while pixels with reach angles $< 30^\circ$ are not at risk. (b)
 892 Calculated reach angles for all pixels surrounding the road network. Inset: closer view of
 893 calculated reach angles for a section of SH1 north of Oaro. (c) Calculated reach angles for all
 894 pixels surrounding the order 3+ river network. Inset: closer view of calculated reach angles for
 895 series of rivers north of Kaikōura.



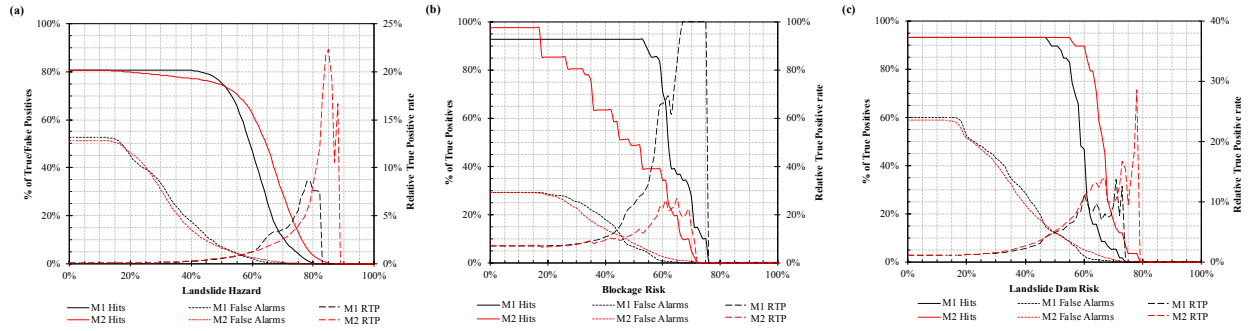
896

897 Figure 4: Model 1 landslide hazard and risk model results based on the USGS ShakeMap®
 898 version 1, completed at 08:30 hrs on 14 November UTC (+0 days 21 hrs 28 mins). (a) input
 899 ground shaking model from USGS; (b) landslide hazard model; (c) landslide road blockage risk
 900 model; (d) landslide dam risk model.



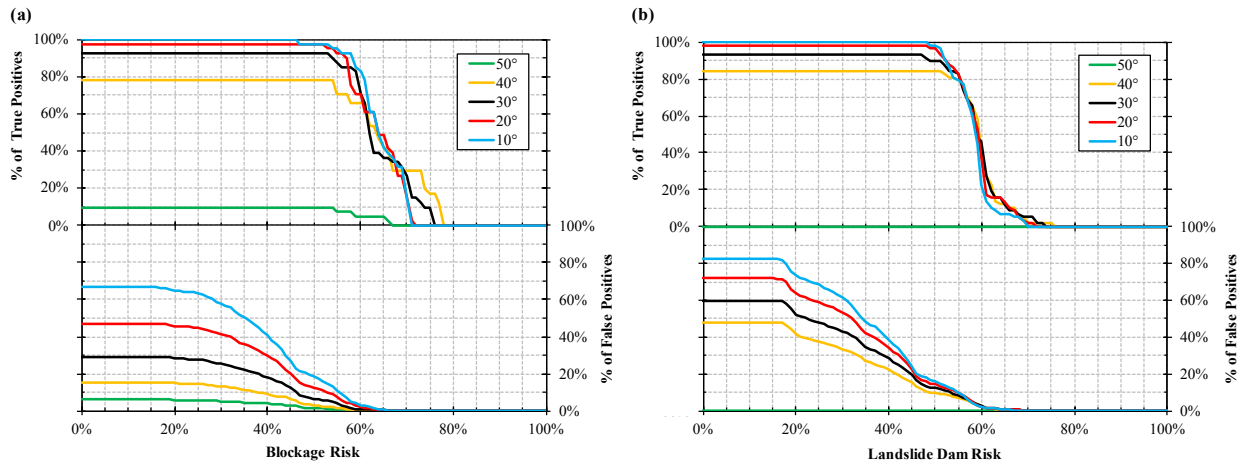
901

902 Figure 5: Model 2a landslide hazard and risk model results based on the GeoNet Shakemap
 903 version 1, completed at 12:30 hrs on 16 November UTC (+3 days 1 hrs 28 mins). (A) input
 904 ground shaking model from GeoNet. The blue halo of low intensity shaking along the entire
 905 coastline resulted from an anomaly in the data processing at the time; (B) landslide hazard
 906 model; (C) landslide road blockage risk model; (D) landslide dam risk model.



907

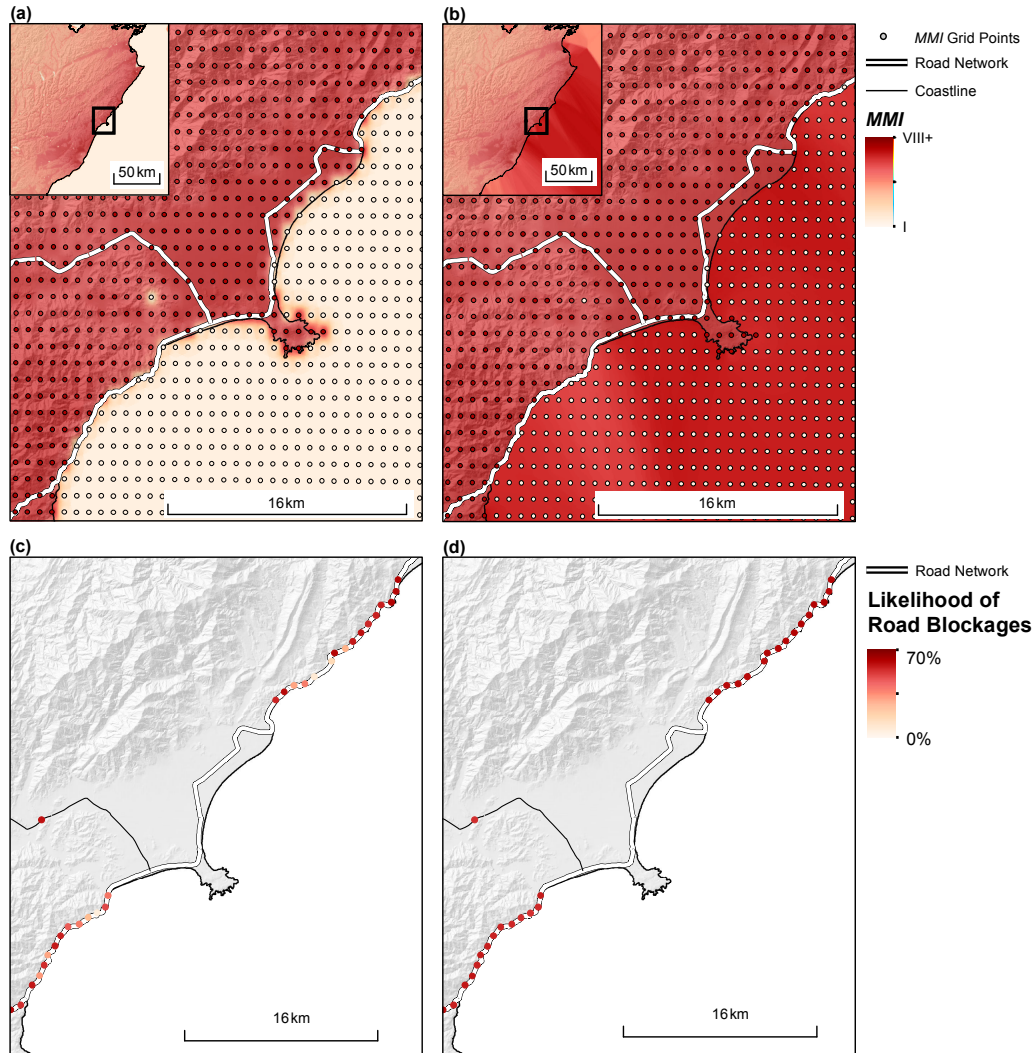
908 Figure 6: Quantitative verification curves showing true positive, false positives, and relative true
 909 positive rates for each of the Model 1 and Model 2 outputs based on initial observed landslides.
 910 (A) landslide hazard outputs; (B), road blockage risk outputs; (C), and landslide dam risk
 911 outputs. True positive curves for road blockages and landslide dams appear step-wise due to the
 912 small number of observed blockages used to verify the models.



913

914 Figure 7: Effect of using different reach angle thresholds on the percentage of true positives and
 915 false positives predicted by Model 1 for road blockages and landslide dams. (A) True and false
 916 positive curves for different reach angle thresholds for road blockage risk; and (B) true and false
 917 positive curves for different reach angle thresholds for landslide dam risk. Decreasing the reach
 918 angle threshold increases the maximum number of hits successfully predicted, but has an

919 associated increase in false alarms. The area between the true and false positive curves for the
920 same threshold angle gives a measure of the best performing threshold value.



921

922 Figure 8: Comparison between *MMI* raster files computed using all grid points in the GeoNet
923 data download and only those grid points located onshore, and the effect on predicted road risk.
924 (A) Interpolated raster file using all grid points; (B) Interpolated raster file using only onshore
925 grid points; (C) Predicted road blockage risk near Kaikōura for Model 2 using *MMI* in (A); and
926 (D) Predicted road blockage risk near Kaikōura for Model 2-corrected using *MMI* in (B).

927 **TABLES**

928 Table 1: Bin ranges and corresponding bin numbers for each of the predisposing factors used in
 929 this study.

Factor	Bin value range	Bin number
Local slope angle (<i>SA</i>)	0-5°	1
	5-10°	2
	10-15°	3
	15-20°	4
	20-25°	5
	25-30°	6
	30-35°	7
	35-40°	8
	40-45°	9
	45-50°	10
	50°+	11
Modified Mercalli Intensity (<i>MMI</i>)	1	1
	2	2
	3	3
	4	4
	5	5
	6	6
	7	7

	8	8
	9	9
	10+	10
Fault proximity (<i>FD</i>)	0-5 km	1
	5-10 km	2
	10-20 km	3
	20-30 km	4
	30-40 km	5
	40-50 km	6
	50+ km	7
River Proximity (<i>RD</i>)	0-0.5 km	1
	0.5-1.0 km	2
	1.0-1.5 km	3
	1.5-2.0 km	4
	2.0-2.5 km	5
	2.5+ km	6
Slope Position (<i>SP</i>)*	Flat	1
	Valley bottoms	2
	Mid-slopes	3
	Ridgelines	4

930 *Slope position is a qualitative measure based on a combination of slope angle, slope curvature, and elevation of
931 neighbouring pixels. The classification in this study follows the example given in Jenness et al. (2013).

932

933 Table 2: Sensitivity analysis for Model 1 road blockage and landslide dam outputs.

Area between true and false positive curves (/1)		
Reach Angle	Roads	Landslide
Threshold	Blockages	Dams
10°	0.36	0.27
20°	0.42	0.30
30°	0.48	0.32
40°	0.46	0.33
50°	0.03	0.00

934